Defect and Diffusion Forum Vol. 331 (2012) pp 181-199
Online available since 2012/Sep/19 at www.scientific.net

doi:10.4028/www.scientific.net/DDF.331.181

Defect Behaviour in Yttria-Stabilised Zirconia Nanomaterials Studied by Positron Annihilation Techniques

Ivan Prochazka[1,a], Jakub Cizek[1,b], Oksana Melikhova[1,c], Jan Kuriplach[1,d], Wolfgang Anwand[2,e], Gerhard Brauer[2,f], Tetyana E. Konstantinova[3,g], Igor A. Danilenko[3,g], Igor A. Yashchishyn[3,g]

[1]Charles University in Prague, Faculty of Mathematics and Physics, Department of Low Temperature Physics, V Holesovickach 2, CZ-180 00 Prague 8, Czech Republic

[2]Helmholtz-Zentrum Dresden-Rossendorf, Institute of Radiation Physics, POB 51 01 19, D-01314 Dresden, Germany

[3]Donetsk Institute for Physics and Engineering named after O. O. Galkin of the NAS of Ukraine, Luxembourg Street 72, 83114 Donetsk, Ukraine

[a]ivan.prochazka@mff.cuni.cz (corresponding author), [b]jakub.cizek@mff.cuni.cz, [c]oksana.melikhova@mff.cuni.cz, [d]jan.kuriplach@mff.cuni.cz, [e]w.anwand@hzdr.de, [f]g.brauer@hzdr.de, [g]matscidep@aim.com

Keywords: Yttria-stabilised zirconia. Chromium doping. Pressure-compacted nanopowders. Sintered ceramics. Positron lifetimes. Coincidence Doppler broadening. Slow positron implantation spectroscopy. Theoretical *ab-initio* calculations of positron parameters.

Abstract. Recent experimental and theoretical investigations on a variety of yttria-stabilised zirconia (YSZ) nanomaterials are reviewed. The investigations were conducted within the frame of a collaboration of three institutions: (i) Charles University in Prague, (ii) Helmholtz Centre Dresden-Rossendorf and (iii) Donetsk Institute for Physics and Engineering of the NAS of Ukraine, Materials studied involved pressure-compacted nanopowders of binary and ternary (with Cr_2O_3 additive) YSZ and YSZ ceramics obtained by sintering the nanopowders. The nanopowders were prepared by the co-precipitation technique. Positron annihilation spectroscopy including the conventional positron lifetime (LT) and coincidence Doppler broadening (CDB) techniques was employed as the main experimental tool. Slow positron implantation spectroscopy (SPIS) was used in investigation of commercial YSZ single crystals for reference purposes. Extended state-of-art theoretical *ab-initio* calculations of positron response in the ZrO_2 lattice were carried out for various vacancy-like defect configurations. It was suggested by these calculations that none of the oxygen-vacancy related defects are capable to trap positrons. On the other hand, zirconium vacancy was demonstrated by the calculations to be a deep positron trap, even in the case that a hydrogen atom is attached to the vacancy. The measured positron LT data clearly indicated that positrons annihilate in nanopowders predominantly from trapped states at defects of two kinds: (a) the vacancy-like misfit defects concentrated in layers along the grain boundaries and characterised with lifetimes of ≈ 0.180 ns, and (b) the larger defects of open volume comparable to clusters of a few vacancies which are situated at intersections of three (or more) grain boundaries (characteristic lifetimes of ≈ 0.380 ns). The intensity ratio of LT components corresponding to these two kinds of defects was found to be correlated with the mean particle size. This correlation reconfirms the above interpretation of LT components and, moreover, the measured ratios could be used to estimate changes of the mean particle size with chromia content or sintering temperature. It was shown in this way that chromia addition to the YSZ nanopowder leads to a smaller particle size compared to the binary YSZ. Similarly, grain growth during sintering could be monitored via this intensity ratio. A portion of ≈ 10 % of positrons was found to form positronium (Ps) in compacted binary YSZ nanopowders. The observed ortho-Ps lifetimes correspond to Ps pick-off annihilation in cavities of ≈ 3 nm size which may be expected to occur between the primary nanoparticles. On the other hand, an addition of chromia at a concentration as low as 0.3 mol.% appeared to be sufficient to suppress Ps formation below the detection limit. Similarly, Ps formation could not be detected in binary YSZ sintered for 1 hour at a temperature of 1000 °C or higher. The former effect indicates an enhanced

concentration of Cr cations at the particle surfaces, while the latter one appears to be due to a decrease of cavity concentration induced by sintering. The measured CDB data supported the idea that vacancy-like trapping centres are similar to zirconium vacancies and gave further evidence of a strong segregation of Cr segregation at particle interfaces.
SPIS was further involved in a trial experiment on binary YSZ nanopowders and sintered ceramics. This experiment clearly demonstrated that SPIS may reveal valuable information about changes of depth profiles of microstructure during sintering, e.g. a sintering induced diffusion of defects from sample interior to its surface.

Introduction

Zirconium dioxide (alternatively termed as zirconia) is a wide band-gap (5.0–5.5 eV) metal oxide which embodies a rare combination of advantageous thermal, electronic, mechanical and chemical properties [1]. First, the melting point of zirconium dioxide is as high as 2750 °C and zirconia exhibits a low thermal conductivity. Likewise, zirconia is a very good high-κ dielectric material showing a low electronic conductivity, but it is a good oxygen ionic conductor at increased temperatures. In addition, zirconia features a high hardness combined with reasonable fracture toughness. Zirconia is also a material of good corrosion and wear resistance. Due to these properties, zirconium dioxide has become the base constituent of materials designed for a wide range of industrial applications, for example, as functional ceramics, ceramic glazes, refractory materials, electroceramics, insulators, solid oxide fuel cells, oxygen sensors, dental implants, machining tools, grinding media and abrasives.

Zirconia can occur in three different crystalline forms [1]: monoclinic (*m*), tetragonal (*t*) or cubic (*c*) ones. The pure ZrO_2 is monoclinic at room temperature, but it undergoes transition to the denser tetragonal phase at a temperature of ≈ 1100 °C. Above a temperature of 1380 °C, the cubic structure of the pure zirconia becomes stable. Due to a greater specific volume of the ZrO_2 monoclinic phase, considerable volume changes occur whenever zirconia passes through the monoclinic-tetragonal phase transformation temperature. Such volume changes can eventually lead to a creation of cracks within the ZrO_2 structure. Indeed, this zirconia polymorphism imposes severe restrictions on exploitation area of the *pure* zirconium dioxide in high temperature applications. A stabilisation of high-temperature zirconia phases is thus an obvious prerequisite of gaining a maximum benefit of favourable features of this attractive material.

It has become known for many years that an immersion of a small amount of a suited metal oxide in a form of a solid solution in ZrO_2 lattice may bring about the stabilisation of high-temperature zirconia phases. Stabilisation effect is generally ascribed to a larger ionic radius, r_{ion}, of the impurity metal atom compared to that of Zr. For instance, the trivalent yttrium oxide (Y_2O_3, yttria) introduced into zirconia lattice is widely used as a phase stabilisation agent [1] ($r_{Zr,4+}$ = 0.084 nm, $r_{Y,3+}$ = 0.105 nm)

The yttria-in-zirconia solid solution is usually referred to as the yttria-stabilised zirconia (YSZ). If the amount of Y_2O_3 immersed into the ZrO_2 host lattice exceeds ≈ 8 mol.% (i.e. ≈ 14 wt.%), the YSZ is termed fully phase-stabilised [1] because its structure remains cubic (*c*-YSZ) from high down to room temperature. An amount of ≈ 3 mol.% (≈ 5.7 wt.%) of Y_2O_3 ,which is insufficient to stabilise the cubic phase, converts the YSZ structure into the tetragonal (*t*-YSZ) one after heating above ≈ 1000 °C temperature [1]. The *t*-YSZ structure, however, is metastable below ≈ 1000 °C temperature, where it may coexist with the monoclinic (*m*-YSZ) one. Thus, the *t*-YSZ is referred to as only partially phase-stabilized. Immersion of the Y_2O_3 into the ZrO_2 host lattice violates the stoichiometry of the YSZ solid solution. As a result, a huge amount of native oxygen vacancies and vacancy – solute atom complexes are created in the lattice. These vacancy-like lattice defects may in turn significantly influence some functional characteristics of the YSZ system.

A mixture of two oxides, like e.g. the yttria–zirconia solid solution, is called a *binary* oxide system. Beside the yttria, several other metal oxides (CaO, MgO) are known to have stabilizing effect on zirconia high-temperature phases if they are introduced into the ZrO_2 lattice as a solid solution [1]. Nowadays, *ternary* zirconia-based solid oxide solutions, containing beside the zirconia

and a phase stabiliser a third metal oxide ingredient, experience growing interest among researchers in physics and industry. An integration of another metal oxide into the YSZ system needs not necessarily magnify a phase-stabilisation effect, but it may influence positively other characteristics of the material, e.g. mechanical properties, ionic conductivity, thermal stability and sintering temperature. The ternary YSZ containing the trivalent chromium oxide (Cr_2O_3, chromia) is currently one of most interesting zirconia-based ternary systems [2] because of a smaller Cr ionic radius ($r_{Cr,3+}$ = 0.076 nm) and a possible multiple Cr valence which may influence e.g. migration of Cr ions and/or grain growth. Below, we shall refer to $ZrO_2 - Y_2O_3 - Cr_2O_3$ solid solutions as the YSZC systems.

When zirconia-based functional materials have been formed from sub-micrometer grained structures, like e.g. ceramics made of nanoparticle powders subjected to pressure compaction and subsequent sintering, they usually gain much improved properties compared to the ordinary coarse-grained materials. A wide range of metal oxide nanopowders with average particle size as low as ≈ 10 nm has become nowadays commercially available or can be easily produced in laboratory conditions. The average size and the size distribution of initial nanoparticles as well as their phase composition are some of important factors which determine functionality and quality of materials resulting from nanopowder processing. All these factors thus should be kept under control. In addition, the volume fractions of grain boundaries (GB's) and particle interfaces (PI's) become important in nanomaterials. The GB's represent a kind of internal surface in the material and they may appear to be of a rather complicated structure which is substantially distinguished from that of the grain interiors. For instance, there may appear open-volume misfit defects associated with GB's. A migration of (impurity) metal atoms toward GB's may take place. As a result, GB's may carry a charge and be accompanied by compensating layers of the opposite charge situated along them. Indeed, an increasing volume fraction of GB's starts to significantly influence various functional properties of the material, for example electronic or ionic conductivity. A thorough characterisation and understanding of all the structure aspects of the YSZ-based nanomaterials should thus be regarded as an essential step toward implementation of these materials in practice.

Positron annihilation spectroscopy (PAS) is nowadays a well-recognised experimental methodology which serves for non-destructive investigations of open-volume structures of a size scale far below 1 micrometer [3,4]. It is evident therefore, that PAS can be a very efficient tool of research on the YSZ-based nanomaterials. In the traditional mode of PAS, referred to as *conventional* PAS, positrons from an appropriate β^+-emitting radionuclide (typically ^{22}Na) are directly implanted into the material under study. At the moment of implantation, a majority of these positrons have a kinetic energy of several hundreds of keV, ranging, moreover, over a broad energy interval. In metals and other dense media, the stopping range of such positrons amounts typically hundreds of micrometers and the positron implantation depth profiles exhibit a pattern which is roughly exponentially decreasing in the material. Thus, no reasonable depth resolution on a sub-micrometer scale is provided by conventional PAS. Only a small fraction of such positrons (<1 %) can diffuse back to the sample surface and get annihilated there. In practice, therefore, conventional PAS has almost no potential for surface studies and depth profiling of microstructure of coarse-grained materials. Conventional PAS conveys a volume information about materials structure since a positron response is integrated over a broad region of about hundreds of micrometer depth probed by positrons. Two main techniques of conventional PAS are currently employed in materials investigations [4]: (a) positron lifetime (LT) measurements which respond to the size of open volume associated to defects capable of positron trapping and the concentrations of these defects and, (b) coincidence Doppler broadening (CDB) measurements which reflect chemical vicinity of the positron annihilation site and provide also integral information about the role of positron trapping.

As far as surface studies and depth profiling of microstructure are considered, conventional PAS cannot compete with *slow-positron implantation* spectroscopy (SPIS) – a technique which utilises monoenergetic positron beams of low energy (< 100 keV) as the source of positrons [5] and becomes thus to be a complementary technique to the conventional PAS. A particular depth interval probed by positrons can be selected by a proper choice of positron energy.

Compared to coarse grained materials, a different situation may occur in nanomaterials. Diffusion lengths of thermalised positrons amount typically a few hundreds of nanometers in nearly perfect metals as well as the other dense media. The average size of particles constituting nanomaterials becomes comparable with or even less than positron diffusion lengths. Thermalised positrons can then easily reach GB's by diffusion and get trapped there prior to annihilation. As far as the volume fraction of GB's becomes significant in a particular nanomaterial, an appreciable portion of positrons can annihilate from a trapped state at GB's and give rise to a different response from that originated in the grain interiors. These two kinds of positron signals may be distinguished experimentally. Thus, the potential of the conventional PAS to serve for *internal surface* studies on nanomaterials may be strongly enhanced due to the positron diffusion mechanism combined with a smaller grain size and the positron trapping power of GB's.

One of the most advanced techniques suitable for the preparation of the zirconia nanopowders is precipitation. It is a widely used chemical method which can produce nanopowders in large amounts. Compared to other methods, the precipitation technique (1) provides a homogenous distribution and incorporation of dopants over nanoparticles and (2) allows for a control of the size and surface of nanoparticles since the oxide nanoparticles are obtained from hydroxide precipitates through calcination. The history of precipitates and calcination processing mode are the most important factors that determine the final size of nanoparticles and the development of their surface.

Over the past five years, a series of PAS investigations on a variety of YSZ-based nanomaterials has been conducted [6–17] within the collaboration between Charles Univ. Prague – Physics and Engineering Inst. Donetsk – Helmholtz Centre Dresden-Rossendorf. Extensive PAS experiments were carried out involving both the conventional PAS (LT and CDB measurements) and SPIS. Comprehensive *ab-initio* theoretical calculations of positron response in YSZ lattice were also performed including a variety of defect configurations. In the present paper, the results of these investigations will be reviewed and some general conclusions will be drawn.

Experimental techniques

Samples. Materials studied in this work can be divided into three groups: (i) pressure-compacted binary and ternary YSZ nanopowders having several different content of yttria or chromia, (ii) ceramics prepared by sintering of the compacted nanopowders at several temperatures, and (iii) reference specimens (an YSZ single crystal, ZrO_2–Cr_2O_3 compacted nanopowder, and relevant pure metals). The phase composition and the mean particle size of initial nanopowders were characterised by means of transmission electron microscopy (TEM) and X-ray diffraction (XRD). All the YSZ-based nanomaterials included under (i) and (ii) were made by Donetsk collaborators and their basic characteristics are listed in Table 1.

Pressure-compacted YSZ nanopowders. The initial binary or ternary YSZ nanopowders for the present investigations were prepared by a modified co-precipitation technique that included a series of physical and chemical treatments applied in order to prevent a formation of hard aggregates. The technique was developed by Donetsk collaborators and described in details elsewhere [2,18,19]. Chemical purity of the initial nanopowders was examined by the X-ray fluorescence analysis and upper limits for impurities were shown not to exceed 0.1 at.% [10]. The initial nanopowders were calcinated at a temperature of 600–700 °C for 1 hour and afterwards subjected to an uniaxial compacting pressure (250, 500, 1000 MPa) at ambient temperature. Compaction resulted in disk shaped specimens of 12–15 mm in diameter and ≈ 5 mm in thickness. The XRD measurements, taken on selected specimens prior to and after pressure compaction, suggested, that the mean particle size was not affected significantly by the compaction.

Sintered YSZ ceramics. YSZ ceramics were made of the pressure-compacted binary *t*-YSZ nanopowders by sintering at three different temperatures T_S = 1000, 1200 and 1350 °C for 1 hour in air followed by controlled cooling at a rate of 2 K/min above 1200 °C temperature. Below this temperature, the samples were cooled down to room temperature in a furnace switched off. All the samples were kept in air and dried for 1 hour at 105 °C in air prior to each measurement. In

addition, a series of ternary *t*-YSZ compacted nanopowders with different content of up to 2.9 mol.% of Cr_2O_3 was prepared and subjected to sintering at 1350 °C and subsequent cooling under the same mode as above.

Table 1. The list of materials studied in the present work. The chemical composition, compacting pressure *P*, phase (*c* – cubic, *t* – tetragonal, *m* – monoclinic), and mean particle size *d* determined by XRD prior compaction are given in the Table.

Material		***P* [MPa]**	**Phase**	***d* [nm]**
Abbrev.	Chemical composition			
Pressure-compacted binary YSZ nanopowders:				
Zr0Y	pure ZrO_2	250	*m*	23 ± 2
		500	*m*	
		1000	*m*	
Zr3Y	ZrO_2+3 mol.% Y_2O_3	250	*t*	18 ± 1
		500	*t*	
		1000	*t*	
Zr8Y	ZrO_2+8 mol.% Y_2O_3	250	*c*	16 ± 1
		500	*c*	
		1000	*c*	
Pressure-compacted ternary YSZ nanopowders:				
Zr3Y0Cr	ZrO_2+3 mol.% Y_2O_3	500	*t*	
Zr3Y0.3Cr	ZrO_2+3 mol.% Y_2O_3+0.3 mol.% Cr_2O_3	500	*t*	18 ± 1
Zr3Y0.7Cr	ZrO_2+3 mol.% Y_2O_3+0.7 mol.% Cr_2O_3	500	*t*	15 ± 1
Zr3Y1.5Cr	ZrO_2+3 mol.% Y_2O_3+1.5 mol.% Cr_2O_3	500	*t*	
Zr3Y2.9Cr	ZrO_2+3 mol.% Y_2O_3+2.9 mol.% Cr_2O_3	500	*t*	12 ± 1
Zr3Y5Cr	ZrO_2+3 mol.% Y_2O_3+5.0 mol.% Cr_2O_3	500	*t*	
*Sintered binary YSZ ceramics *:*				
$Zr3Y_0$	ZrO_2+3 mol.% Y_2O_3	500	*t*	
$Zr3Y_{1000}$	ZrO_2+3 mol.% Y_2O_3	500	*t*	35 ± 3
$Zr3Y_{1200}$	ZrO_2+3 mol.% Y_2O_3	500	*t*	
$Zr3Y_{1350}$	ZrO_2+3 mol.% Y_2O_3	500	*t*	
*Sintered ternary YSZ ceramics *:*				
$Zr3Y0Cr_{1350}$	ZrO_2+3 mol.% Y_2O_3	500	*t*	
$Zr3Y0.3Cr_{1350}$	ZrO_2+3 mol.% Y_2O_3+0.3 mol.% Cr_2O_3	500	*t*	
$Zr3Y0.7Cr_{1350}$	ZrO_2+3 mol.% Y_2O_3+0.7 mol.% Cr_2O_3	500	*t*	
$Zr3Y1.5Cr_{1350}$	ZrO_2+3 mol.% Y_2O_3+1.5 mol.% Cr_2O_3	500	*t*	
$Zr3Y2.9Cr_{1350}$	ZrO_2+3 mol.% Y_2O_3+2.9 mol.% Cr_2O_3	500	*t*	

* Sintering temperature T_S in °C is specified as the subscript of sample abbreviations in the 1st column (subscript 0 denotes virgin compacted nanopowder).

Reference specimens. For comparison purposes, a *c*-YSZ (ZrO_2+9 mol.% Y_2O_3, manufactured by Crystec, GmbH) and *t*-YSZ (ZrO_2+3 mol.% Y_2O_3) single crystals were studied. These specimens are abbreviated below as Zr9Ysc and Zr3Ysc, respectively. In addition, pure Zr, Y and Cr well-annealed high-purity metals were investigated in order to facilitate interpretation of data measured by the CDB technique. All these three pure metals were verified by LT measurements to be essentially defect-free materials in which virtually all positrons annihilate from the delocalised state.

A ZrO_2+3 mol.% Cr_2O_3 compacted nanopowder was also studied. The material was prepared by a co-precipitation technique similar to that used for the other nanopowders and served for comparison with the results obtained on the ternary YSZ systems.

Conventional PAS – apparatus and data acquisition. All the conventional PAS measurements were carried out in the PAS laboratory in Prague. The measurements were conducted at ambient temperature in air.

Positron sources. Carrier-free ^{22}Na activity in carbonate or chloride form supplied by iThemba Labs was utilised for preparation of positron sources used in conventional PAS measurements. A drop of water solution of the salt containing ≈ 1.3 MBq of activity was dried and sealed between two mylar C foils (DuPont) of 4 μm in thickness. The source was then sandwiched with two identical pieces of the material studied.

LT measurements. LT measurements were executed using the fast–fast arrangement of a BaF_2 positron lifetime spectrometer [20] which exhibited a time resolution of ≈ 165 ps (FWHM for ^{22}Na), a coincidence count rate of ≈ 100 s^{-1} and a ratio of peak to background (PBR) of ≈ 10^3. During later stages of these measurements, a digital BaF_2 LT spectrometer [21] was also employed, which operated with improved time resolution of 140 ps (FWHM for ^{22}Na). In each measured LT spectrum, at least 10^7 true coincidence events were accumulated. LT spectra were decomposed into discrete components using a maximum likelihood procedure [22].

CDB measurements. In CDB measurements, a CDB spectrometer involving two HPGe detectors and analogue NIM modules was employed. The spectrometer exhibited an energy resolution of 1.0 keV (FWHM) at the 511 keV γ-ray energy, a coincidence count rate of ≈ 500 s^{-1} and a PBR better than 10^5. In later experiments, a digitised configuration of the CDB spectrometer [23] was utilised. Two-dimensional energy spectra containing at least 10^8 coincidence events were recorded in each CDB measurement. Doppler-broadened profiles (DBP's) of annihilation radiation were then extracted from the raw CDB spectra and related to the DBP of the Zr reference specimen. The Doppler broadened shapes of the annihilation peak were also characterised with the ordinary *S* (sharpness) and *W* (wing) parameters.

SPIS measurements. SPIS measurements were performed using a magnetically guided monoenergetic positron beam – the SPONSOR facility [24] at Rossendorf. Positron energies E_+ covered the region from 30 eV to 35 keV. The beam spot diameter was ≈ 4 mm for each of selected values of E_+. Energy spectra in the annihilation region were measured with a HPGe detector of a ≈ 30 % efficiency which exhibited an energy resolution of 1.06 keV (FWHM) at the 511 keV γ-ray energy. At least 5×10^5 counts were accumulated in each spectrum. The *S* and *W* parameters were calculated and then analysed as functions of E_+ using the VEPFIT code [25].

Survey of experimental data

In this Section, experimental data collected in the present investigations are briefly surveyed. The reader is referred to our publications [6–17] for full presentations of the measured data. Microstructure information derived from these data is surveyed in the later in this review.

Conventional PAS. *Positron lifetime data.* Up to four discrete components arising from annihilation of positrons in YSZ materials could be resolved after positron source contribution was extracted [6,10,15]. These components could be distinguished into two groups:

(a) LT components exhibiting positron lifetimes below 0.5 ns. The components of this group should be attributed to annihilation of positrons that had not formed ortho-Ps (oPs).

(b) LT components with lifetimes greater than 1 ns. These components were observed only in the compacted binary YSZ nanopowders, but not in materials containing Cr_2O_3 nor in binary YSZ ceramics, sintered at $T_S \geq 1000$ °C. Obviously, such components originated from oPs pick-off annihilations. Contribution of para-Ps (pPs) components (τ_{pPs} = 0.125 ns) were subtracted.

Table 2. Measured positron lifetimes and relative intensities, τ_i and I_i, respectively, observed on binary and ternary compacted YSZ nanopowders and sintered ceramics in the region of $\tau_i < 1$ ns. Relative intensities are normalised as described in the text. The 1 standard deviation is given in parentheses in the units of the last significant digit. Data of the Table were taken from Refs. [6,10,15].

Material *	τ_1 [ns]	I_1 [%]	τ_2 [ns]	I_2 [%]	τ_3 [ns]	I_3 [%]
Pressure-compacted binary YSZ nanopowders:						
Zr0Y			0.187(3)	42(2)	0.377(4)	48(2)
Zr3Y			0.174(3)	27(2)	0.373(3)	63(2)
Zr8Y			0.185(3)	30(2)	0.365(4)	60(2)
Pressure-compacted ternary YSZ nanopowders:						
Zr3Y0Cr			0.178(3)	28(2)	0.374(3)	61(2)
Zr3Y0.3Cr			0.191(3)	31.4(9)	0.381(2)	68.6(9)
Zr3Y0.7Cr			0.191(3)	26.0(8)	0.390(2)	74.0(8)
Zr3Y2.9Cr			0.209(2)	20(1)	0.398(5)	80(1)
Zr3Y5Cr			0.260(10)	20(1)	0.393(4)	80(2)
Sintered binary YSZ ceramics:						
$Zr3Y_0$			0.186(3)	30(1)	0.382(2)	60(1)
$Zr3Y_{1000}$			0.185(2)	77(1)	0.374(2)	23(1)
$Zr3Y_{1200}$			0.185(1)	99(1)	≈ 0.374	1(1)
$Zr3Y_{1350}$	0.035(9)	7(1)	0.178(1)	93(1)		
Sintered ternary YSZ ceramics:						
$Zr3Y0Cr_{1350}$	0.40(10)	5(2)	0.176(2)	88(1)	0.322(9)	7.2(6)
$Zr3Y0.3Cr_{1350}$	0.36(9)	4(1)	0.176(4)	91(1)	0.357(9)	5.0(5)
$Zr3Y0.7Cr_{1350}$	0.35(9)	6(2)	0.1767(8)	90(2)	0.380(10)	4.0(5)
$Zr3Y1.5Cr_{1350}$	0.40(10)	4(1)	0.176(1)	91.6(5)	0.363(9)	4.4(2)
$Zr3Y2.9Cr_{1350}$	0.40(10)	5(3)	0.1768(8)	89(3)	0.380(9)	5.7(2)

* Material abbreviations coincide with those in the 1st column of Table 1.

Table 3. Measured positron lifetimes and relative intensities, τ_i^{oPs} and I_i^{oPs}, respectively, originated from oPs annihilations in binary compacted YSZ nanopowders. Relative intensities are normalised as described in the text. The 1 standard deviation is given in parentheses in the units of the last significant digit. Data of the Table were taken from Refs. [6,10]

Material *	P [MPa]	τ_1^{oPs} [ns]	I_1^{oPs} [%]	τ_2^{oPs} [ns]	I_2^{oPs} [%]
Z0Y	250	1.9(1)	1.8(1)	31(2)	6.3(3)
	500	1.8(1)	1.5(1)	31(2)	5.7(3)
	1000	2.0(1)	2.3(1)	31(2)	6.0(3)
Z3Y	250	2.0(2)	1.2(1)	31(2)	5.4(3)
	500	1.6(1)	1.4(1)	30(2)	5.9(3)
	1000	1.7(1)	2.0(1)	28(2)	7.1(3)
Z8Y	250	2.0(2)	1.2(1)	30(2)	5.5(3)
	500	2.2(1)	2.1(1)	26(2)	5.0(3)
	1000	2.2(2)	1.6(1)	31(2)	5.9(3)

* Material abbreviations coincide with those of Tab. 1, the 1st column.

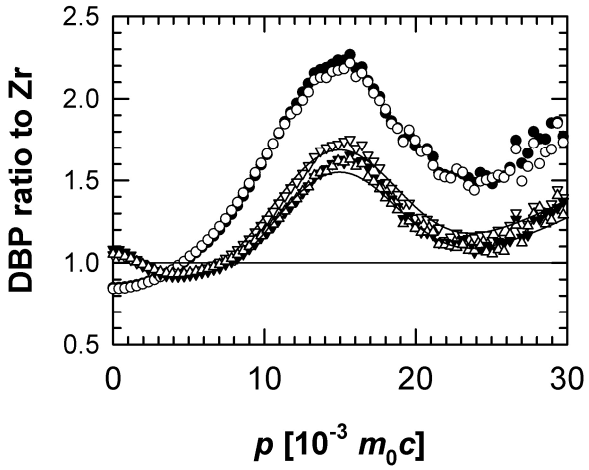

Fig. 1. The measured DBP ratio curves for binary YSZ compacted nanopowders: ∇ – Zr0Y, ▼ – Zr3Y, Δ – Zr8Y. DBP curves for the reference single crystals are also plotted: ● – Zr3Ysc, ○ – Zr8Ysc. The solid lines represent DBP ratios for Zr0Y and Zr8Y calculated within the model described in Ref. [10].

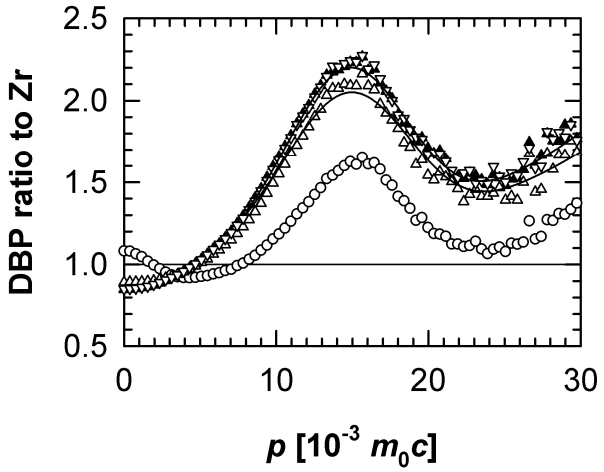

Fig. 2. The measured DBP ratio curves for binary t-YSZ sintered ceramics: Zr3Y (virgin nanopowder, ○), Zr3Y1000 (Δ), Zr3Y1200 (∇). DBP curve for the reference Zr3Y single crystal is also plotted (▲). The solid lines represent DBP ratios for T_S = 1000 and 1200 °C calculated within the model described in Ref. [10].

In Table 2, lifetimes and relative intensities (τ_i and I_i, respectively, i=1,2,3) of individual LT components belonging to group (a) were listed (only data on materials pressed under 500 MPa were included in the Table). Table 3 contains LT data on components appertaining to group (b): lifetimes τ_i^{oPs} and relative intensities I_i^{oPs}, i=1,2. Common normalisation of relative intensities contained in Tables 2 and 3 is performed so that $I_1+I_2+I_3+4(I_1^{oPs}+I_2^{oPs})/3=100$ %.

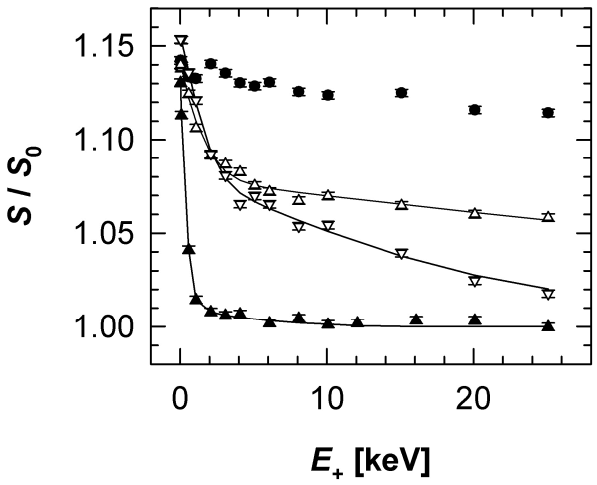

Fig.3. The *S* parameters measured for the binary *t*-YSZ sintered ceramics as a function of positron energy E_+: Zr3Y virgin nanopowder (●), $Zr3Y_{1000}$ (Δ) and $Zr3Y_{1200}$ (∇). The reference curve measured for the Zr9Y single crystal (▲) was also plotted. *S*-values were normalised to the bulk *S* measured for the Zr9Ysc specimen. Solid lines represent VEPFIT fitted curves obtained in Ref. [16].

Coincidence Doppler broadening data. CDB measurements were conducted for the binary and ternary YSZ compacted nanopowders (pressure P=500 MPa) as well as binary YSZ ceramics. In order to assist to a unique interpretation of CDB data measured on such complicated systems, CDB spectra were also taken for the Zr9Y single crystal and the pure metal reference materials (Zr, Y and Cr). Full presentations of measured DBP ratios (related to the Zr reference material) were published in Refs. [9,10,13]. Here, only two examples of CDB spectra were shown for illustration (Figs. 1 and 2).

Slow positron implantation data. SPIS experiments were conducted on Zr9Y single crystal reference specimen [10] and on a series of binary YSZ's subjected to sintering: Zr3Y$_{Ts}$ [16]. In Fig. 3, measured *S* parameters are plotted as function of positron energy E_+ .

Theoretical calculations of positron response in YSZ lattice

As stated in the Introduction, a huge amount of oxygen vacancies is generated in the YSZ lattice due to a stoichiometry violation resulting from yttria addition. These vacancies may stay isolated or agglomerate into a variety of more complicated defect configurations, like e.g. divacancies or vacancy–metal atom complexes. In order to investigate the positron trapping capability of various kinds of defects and to examine simultaneously PAS power to detect these defect types, theoretical considerations, based on the first-principle *ab-initio* calculations, were taken into account. Extended theoretical calculations were, therefore, performed as part of the present investigations, including positron binding energies to defects, E_b , positron lifetimes, τ_c , and momentum distributions of annihilation photons. For a detailed description of these calculations and a full presentation of results, the reader is referred to our earlier publications [7,10,11,12] in which several calculation schemes were also examined. The summary in this Section is confined to the starting points of the calculation schemes and a brief characterisation of theoretical results; the consistency of the experimental results with the calculations is treated in the next Section.

Let us recognise the types of point defects that can be expected in the YSZ lattice. One has to realise that yttrium ions substitute zirconium ones. This substitution results in the creation of oxygen vacancies compensating electrostatically the lattice. We will use below the Kröger – Vink notation [26] in which the Zr^{4+} ion is denoted as $Zr^{\bullet\bullet\bullet\bullet}$, the substituting Y^{3+} ion as Y_{Zr}' and the oxygen vacancy, V_O^{2+}, as $V_O^{\bullet\bullet}$. Note that Y_{Zr}' bears −1 charge relative to the lattice while $V_O^{\bullet\bullet}$ is doubly positively charged. It means first that an attractive force exists between Y_{Zr}' and $V_O^{\bullet\bullet}$. To keep the lattice electrically neutral, two Y_{Zr}' ions are necessary per one $V_O^{\bullet\bullet}$. On the basis of the former experimental and theoretical knowledge about YSZ microstructure, discussed in detail in Ref. [10], an isolated $V_O^{\bullet\bullet}$, the $Y_{Zr}'V_O^{\bullet\bullet}Y_{Zr}'$ mono-vacancy complex and the $2Y_{Zr}'V_O^{\bullet\bullet}Zr_{Zr}^{\times}V_O^{\bullet\bullet}2Y_{Zr}'$ divacancy agglomerate with $V_O^{\bullet\bullet}$s aligned along the ⟨1 1 1⟩ direction, were considered as the main oxygen vacancy related defects in the YSZ materials and were thus included in calculations. In the latter two defect complexes, the Y_{Zr}' substitute occupied the next nearest neighbour (NNN) site with respect to $V_O^{\bullet\bullet}$. Calculations further comprised the zirconium vacancy, V_{Zr}'''', and the perfect ZrO_2 lattice. In order to examine a possible influence of a relatively high concentration of oxygen vacancies, which are known from literature to exhibit a tendency to an alignment, some superstructure of $V_O^{\bullet\bullet}$ defects ordered due to an interaction between closely spaced oxygen vacancies was modelled in [10] and was also involved in the calculations.

As the simplest calculation scheme, the case of a *rigid* lattice was considered when atomic relaxations around defects were neglected. The ATSUP method [27,28] was employed for construction of the effective positron potential. Electron-positron correlations were taken into account within the Boroński and Nieminen (BN) approach [29] or gradient-correction (GC) scheme [30]. The defects studied were considered as neutral, i.e., the charge state of the defect was not considered in this scheme. Results calculated within this simple scheme revealed very small differences in positron parameters which were found independent of phase (*t* or *c*) [10]. In Table 4, an example illustrating calculated data in the case of the rigid lattice is given (columns 2 and 3). It can be seen from the Table that none of the oxygen vacancy related defects considered in the calculations is capable of positron trapping due to insufficient positron binding energy. In contrast

to the oxygen vacancy-like defects, V_{Zr}'''' was nominated by these calculations to be a strong positron trap with a binding energy of E_b=2.7 eV. One can also note that, as expected, the $V_O^{\bullet\bullet}$ superstructure prolonged the positron lifetimes compared to an isolated $V_O^{\bullet\bullet}$ as well as to the perfect lattice, see Table 4.

Table 4. The ATSUP calculations with BN approach for electron-positron correlations of positron binding energy to defect, E_b , and positron lifetime, τ_c , for positrons in the cubic ZrO_2 lattice. Data in the Table are taken from Ref. [10].

Annihilation site	*non-relaxed defect geometry*		*relaxed defect geometry*			
			charge transfer neglected		*charge transfer involved*	
	E_b **[eV]**	τ_c **[ns]**	E_b **[eV]**	τ_c **[ns]**	E_b **[eV]**	τ_c **[ns]**
$V_O^{\bullet\bullet}$	0.02	0.140	0.01	0.139	−0.12	0.132
$Y_{Zr}'V_O^{\bullet\bullet}Y_{Zr}'$	<0.01	0.138	0.30	0.164	0.04	0.139
$2Y_{Zr}'V_O^{\bullet\bullet}Zr_{Zr}^{\times}V_O^{\bullet\bullet}2Y_{Zr}'$	0.02	0.144	0.20	0.156	0.01	0.134
V_{Zr}''''	2.72	0.196	2.75	0.216	2.80	0.220
$V_O^{\bullet\bullet}$ superstructure		0.153				
perfect lattice		0.138		0.138		0.133

A more sophisticated calculation scheme was then applied which allows for *lattice relaxations* around defects. Such relaxations are known from literature data to take place in oxides. To find out relaxed defect geometries, the Vienna *ab-initio* simulation package (VASP) [31,32] was employed. A detailed description of these calculations was given in Ref. [10]. The calculated pattern of ionic displacements did not look simple, but the following general conclusions could be outlined [10]. In the cases of an isolated $V_O^{\bullet\bullet}$ and the $2Y_{Zr}'V_O^{\bullet\bullet}Zr_{Zr}^{\times}V_O^{\bullet\bullet}2Y_{Zr}'$ complex, a mutually similar picture is obtained: oxygen atoms at the NNN sites and zirconium nearest neighbour (NN) atoms are relaxed toward the vacancy. This is in contrary to the $Y_{Zr}'V_O^{\bullet\bullet}Y_{Zr}'$ defects which exhibit a more complicated displacement picture tending to destabilise the cubic structure and create a configuration resembling the tetragonal one. Also a V_{Zr}'''' generates opposite displacements: the NN oxygen cations exhibit an outward relaxation, as expected, while the NNN zirconium atoms move toward the vacancy.

In the calculations made for the relaxed defects, two approaches were utilised in [10]:

(i) The conventional ATSUP scheme with the effective positron potential constructed as a superposition of electron densities and Coulomb potentials of free atoms placed at the relaxed positions obtained using VASP. Note that the charge transfer among atoms and, consequently, ionic character of the lattice, are neglected in this case.

(ii) The inclusion of the charge transfer through solving the one-particle Schrödinger equation for a positron in an effective potential, derived from the self-consistent electron density, and the Coulomb potential generated for the VASP determined relaxed defect geometry.

Positron binding energies and positron lifetimes obtained using the relaxed lattice approaches (i) and (ii) are illustrated in Table 4, columns 4, 5 and 6, 7, respectively. It can be immediately seen from the Table that an isolated $V_O^{\bullet\bullet}$ becomes an even less efficient trapping centre for positrons, compared to the non-relaxed case (columns 4, 5 of the Table) due to an open volume reduction by the inward relaxation of neighbour NN (zirconium) and NNN (oxygen) atoms. As a result, positron lifetime for the relaxed $V_O^{\bullet\bullet}$ approaches closely to that of the perfect lattice and positron binding energy becomes negligible. This effect is even more enhanced when the charge transfer is taken into account as in approach (ii), see columns 5, 6 of the Table. In the case of the $Y_{Zr}'V_O^{\bullet\bullet}Y_{Zr}'$ and $2Y_{Zr}'V_O^{\bullet\bullet}Zr_{Zr}^{\times}V_O^{\bullet\bullet}2Y_{Zr}'$ defect complexes, the open volume associated with these complexes is increased due to dominating outward relaxation of NN zirconium atoms. This leads to an increase of calculated E_b- and τ_c-values when charge transfer is neglected. Due to Coulomb repulsion between positron and $V_O^{\bullet\bullet}$, however, these defect complexes become again not capable of positron trapping and positron lifetime is decreased when charge transfer is included in calculations. The

relaxed V_{Zr}'''' becomes a slightly deeper positron trap with a prolonged τ_c, compared to the unrelaxed case. Contrary to the $V_O^{\bullet\bullet}$-related defects, the calculated positron binding energy and positron lifetime are slightly increased when charge transfer in the vicinity of V_{Zr}'''' is switched on. This happens due to a more complicated pattern of charge redistributions around V_{Zr}'''' leading to a lower electron density inside the vacancy; see Ref. [10] for details.

In addition to the open volume defects examined above, a vacancy agglomerate obtained by removing two ZrO_2 units from the lattice was considered in LT calculations. Such an agglomerate can emulate open volume structures expected to occur in compacted nanopowders at interfaces of three or more GB's. The calculated positron lifetime is 0.378 ns, which appears to be in reasonable proximity to the experimental results discussed later in the next Section.

As pointed out above in this Section, the oxygen vacancy possesses charge +2 relative to the lattice. Similarly to other oxides, a formation of single occupied F^+ or neutral F centres via capturing electrons by $V_O^{\bullet\bullet}$ may be considered. However, the present ATSUP calculations for a rigid lattice [10] simultaneously illustrated that oxygen vacancy likely does not give rise to a positron trap even as the single occupied F^+ nor as the neutral F centre.

The momentum distributions of annihilation photons were calculated in the frame of the ATSUP based approach developed in Ref. [33,34]. It should be emphasised that this approach allows for correct inclusion of inner-shell electrons only, because their states are practically uninfluenced by crystal bonding. Conversely, a contribution of valence electrons cannot be accurately computed within this approach. A comparison of the calculated momentum distributions with the experiment is, therefore, reasonable only in the high-momentum part (HMP) of the distribution, where annihilations with core electrons dominate, i.e. in the momentum region $p>10\times10^{-3}\ m_0c$. Detailed descriptions of the calculations were given elsewhere [10]. Two common features of calculated HMPs can be outlined herein:

- A pronounced peak arising from annihilations with oxygen $2p$ electrons occurred at $p \approx 15\times10^{-3}\ m_0c$. The following fractions of positrons annihilating with oxygen electrons could be estimated from the calculations, viz. ≈70 % for V_{Zr}'''', ≈50 % for perfect ZrO_2 lattice and slightly below 50 % for $V_O^{\bullet\bullet}$.
- A contribution of positron annihilations with Y electrons was found by the calculations to be extremely small and, hence, hardly recognised experimentally.

The vacancy agglomerate considered above in this Section, to emulate the possible open space expected at triple junctions of GB's, was also examined in the HMP calculations. From these calculations, it could be estimated that ≈30 % of positrons localised in such agglomerates are annihilated by oxygen electrons [10].

Discussion of experimental data

Zr9Y single crystal. PAS data obtained for the Zr9Y single crystal appeared to have important impact for a unique interpretation of experimental data collected on the other YSZ materials studied in this work which exhibit more complex structures. This is why we shall start this Section with a survey of conclusions inferred from the single crystal results.

The LT measurements on Zr9Ysc material revealed a single component spectrum exhibiting a lifetime of 0.175±0.001 ns [10]. This lifetime is considerably higher than the values of 0.133 to 0.138 ns calculated [10] for delocalised positrons, see Table 4, suggesting thus a dominating role of positron trapping in a single kind of defects. Simultaneously, the experimental positron lifetime is significantly shorter than that calculated for V_{Zr}'''', which was identified by the same calculations as the only reasonable positron trapping centre in the YSZ lattice. Obviously, the nature of positron traps in Zr9Y single crystal deserves greater attention.

The SPIS measurements on the Zr9Y single crystal [10] revealed an extremely short positron diffusion length of $L_+ = 8.6\pm0.4$ nm. This should be again regarded as a clear evidence of saturated positron trapping. The concentration of defects responsible for such trapping was estimated to be as high as ≈ 2 at.%. Note that very short L_+-values were found in similar single crystals also by others [35].

The most pronounced feature of CDB spectra measured on the Zr9Y single crystal [10] was a strong peak centred at an electron momentum of $p \approx 15\times10^{-3}\ m_0c$. Such peaks are known to arise in many metal oxides from positron annihilations with $2p$ oxygen electrons. The dominating fraction of positron annihilations with oxygen electrons again favours positron trapping in V_{Zr}''''-like defects, i.e. defects which chemical surrounding is similar to V_{Zr}'''' with eight NN oxygen atoms.

It seems thus plausible that the trapping centre responsible for positron trapping in Zr9Y single crystal is a defect resembling V_{Zr}''''. Possible reasons for shortening the observed lifetime compared to that calculated for V_{Zr}'''' could be seen in (i) inward relaxation of oxygen anions due to attractive Coulomb force toward the trapped positron, or (ii) the formation of a V_{Zr}'''' complex with an impurity atom, likely hydrogen, which may diminish the open volume associated with the vacancy. Hydrogen effects in Zr9Y single crystal were further investigated by Melikhova et al. [11,12]. It was demonstrated by theoretical calculations, involving atomic relaxations and charge transfer effects, that experimental lifetimes in this system may be explained by positron trapping in zirconium vacancies containing a hydrogen atom. In particular, such a hydrogen – vacancy complex remains capable of positron trapping and the positron lifetime becomes shortened to 0.175 ns, which agrees well with the lifetime observed in the Zr9Y single crystal.

Binary YSZ compacted nanopowders. *LT results.* It can be seen from Tables 2 and 3 that the LT results on the binary YSZ compacted nanopowders exhibit practically no variations of positron lifetimes and intensities with the compaction pressure applied. It suggests that pressure compaction of nanopowders reached a saturation level above 250 MPa. The variations of LT experimental data on the chemical composition of materials display, however, a more diverse pattern. On one hand, positron lifetimes τ_2 and τ_3 of Table 2 as well as both oPs lifetimes of Table 3 show only minor variations indicating close similarities among positron annihilation sites corresponding to a particular lifetime component independently of yttria content. On the other hand, intensities I_2 and I_3 of Table 2 exhibit well-pronounced changes pointing out to large changes in concentrations of corresponding annihilation sites.

A consistent interpretation of the experimental data on the two shortest LT components was described in details in Ref. [10]. Positron lifetimes $\tau_2 \approx 0.185$ ns can obviously be attributed to positrons trapped in vacancy-like defects, i.e. defects associated with an open volume similar to that of a monovacancy, while lifetime $\tau_3 \approx 0.380$ ns corresponds to annihilations of positrons localised in larger defects of open volume comparable to a cluster of a few vacancies. Since the diffusion length of thermalised positrons in YSZ compacted nanopowders is expected [10] to be higher than or at least comparable to mean particle size d found by XRD for the YSZ nanopowders (see Table 1), positrons can easily reach GB's by diffusion and get trapped in defects associated to GB: (i) in vacancy-like misfit defects (τ_2-component) or (ii) in larger defects situated at the junctions of three or more GB's, which are referred to here as triple points (τ_3-component). Since it is natural to assume the vacancy-like misfit defects to be homogeneously spread out along the particle surface, their volume concentration, C_V , should be proportional to the specific GB area, i.e the integral area of GB's per unit volume ($C_V \sim d^{-1}$). Similarly, volume concentration of triple points, C_t , is proportional to an average number of grains per unit volume ($C_t \sim d^{-3}$). Since intensity ratio, I_3/I_2 , depends linearly on concentration ratio C_t/C_V , one can write [10]

$$\frac{I_3}{I_2} = \frac{q^2}{d^2}\ , \tag{1}$$

where q^2 stands for the proportionality constant. In Fig. 4, experimental ratios I_3/I_2 were plotted versus the inverse square of mean particle size d whenever it was known from XRD spectra (Table 1). A linear correlation between the experimental I_3/I_2 and d^{-2}, starting from the coordinate origin, is clearly visible from the Figure, supporting thus the above interpretation of observed τ_2- and τ_3-components. A least-squares fit of quotient q^2 to the data on binary YSZ nanopowders (open circles in the Figure) was performed [6,10] resulting in the value of $q^2 = 576\pm96$ nm^2. The fitted linear dependence is displayed in the Figure by a solid line.

The applicability range of Eq. 1 was further examined in Refs. [6,9,10,15]. First, several data points on the ternary YSZ nanopowders with different content of Cr_2O_3 (triangles up) and sintered binary YSZ nanopowders (triangles down) are also included in the Figure. These data illustrate another way of possible use of Eq. 1, i.e. its predictive power: (1) Relative changes of the mean particle size can be immediately read from plots similar to that of Fig. 4. (2) In the case when XRD data on a particular YSZ nanomaterial are not available, mean particle size may be estimated by inserting LT data into Eq. 1.

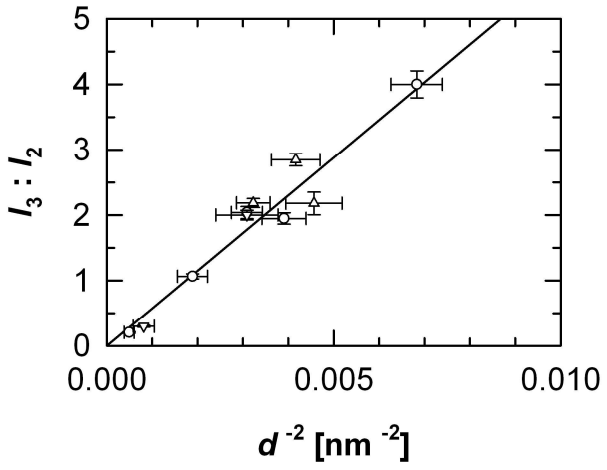

Fig. 4. Ratios I_3:I_2, extracted from LT measurements, plotted against inverse square of mean particle size d, deduced from XRD spectra:
○ – calibration data described in text,
Δ – ternary YSZ compacted nanopowders,
∇ – sintered binary YSZ materials.
The solid line represents a fit of Eq. 1 to calibration points.

In all binary YSZ nanopowders studied, it was found that about 10 % of positrons form Ps. This is clearly evidenced by two oPs lifetime components in the lifetime region above 1 ns [6,10], see Table 3. The main oPs components of the Table, $\tau_2^{oPs} \approx 30$ ns and $I_2^{oPs} \approx 6$ %, should be attributed to oPs pick-off annihilations in larger cavities which are expected to appear between primary nanoparticles [36]. The average size of such cavities can be estimated as ≈3 nm in diameter using semiempirical correlation between the oPs pick-off lifetime and the cavity size [37]. This estimate is in accordance with expectations implied from the aggregate model [36] for ≈ 20 nm diameter primary particles. The shorter (and much weaker) lifetime component of Table 3, $\tau_1^{oPs} \approx 2$ ns and $I_1^{oPs} \approx 2$ %, can be attributed to oPs annihilations in smaller voids of ≈ 0.6 nm size. However, an alternative reason for this component may arise as an artifact of a finite-width lifetime distribution of the main oPs component. Note also that ≈ 1 % of positrons, i.e. about 20 % of those positrons that formed oPs, is estimated to annihilate via the oPs 3γ decay.

CDB results. All DBP ratios obtained for the binary YSZ compacted nanopowders exhibited two clearly visible patterns illustrated in Fig. 1: (i) distinct peaks centred around electron momentum $p \approx 15\times10^{-3}\ m_0c$ which are known to arise in metal oxides from positron annihilations with 2p oxygen electrons, and (ii) an enhancement of the ratios in a close vicinity of zero momentum. The latter pattern finds its origin in para-Ps (pPs) self-annihilations and becomes negligible in high-momentum regions ($p > 10\times10^{-3}\ m_0c$).

Analysis of the measured DBP ratios was described at length in [10]. In this review paper we confine on suppositions made in and conclusions implied by this analysis. The analysis started from an assumption that the total DBP is composed of contributions from four positron states recognised in LT measurements: positrons trapped in (i) vacancy-like defects or (ii) triple junctions, positrons that formed Ps and annihilated via (iii) pPs self-annihilation or (iv) oPs pick-off proces. The relative intensities of particular components of the DBP were taken from LT spectra decompositions. The additional two plausible conditions were also involved in the analysis:

- The oPs pick-off annihilations resemble the DBP of ZrO_2 bulk with approximately equal contributions of oxygen and zirconium electrons.
- The chemical surrounding of vacancy-like defects is similar to that of $V_{Zr}^{''''}$.

Combining theoretical calculations of HMP's (see also the preceding Section) with CDB measurements on Zr9Y single crystal [10], the expected shapes of DBP ratios could be modelled for all the three kinds of the binary YSZ compacted nanopowders. A consistent description of experimental data in the HMC region of $p > 10\times10^{-3}\ m_0c$ could be obtained in this way with virtually no adjusted parameters, supporting thus the adopted interpretation of LT data and confirming simultaneously that yttrium contribution lies under detection limit. The latter finding is in accordance with theoretical estimate as well as CDB measurement on reference Y sample.

Ternary YSZ compacted nanopowders. *LT measurements.* Similar to the case of the binary YSZ compacted nanopowders, two lifetime components arising from positron annihilations in the ternary *t*-YSZ nanopowders could be resolved in the region below 0.5 ns [15], see Table 2. This affords a similar interpretation of these components as in the binary systems: (i) saturated positron trapping in defects takes place also in the ternary YSZ nanopowders with chromia additive, (ii) the shorter lifetime, $\tau_2 \approx 190\div250$ ns, originates from positron trapping in vacancy-like misfit defects that are situated along GB's, and (iii) the longer lifetime, $\tau_3 \approx 360\div390$ ns, occurs due to positrons localised in triple points. It can be seen in the Table that both positron lifetimes exhibit a systematic increase with chromia content what is especially pronounced in τ_2-values. A slight increase of τ_2 for the ZrO_2+3 mol.% Cr_2O_3 compacted nanopowder, compared to the Zr3Y nanopowder, was also observed [15]. It is thus likely that Cr ions slightly increase the size of the vacancy-like misfit defects at GB's, probably due to a smaller ionic radius of Cr than that of Zr. As discussed in Ref. [15], these LT results provide evidence that a segregation of Cr cations at GB's takes place, since annihilation of positrons at GB's dominates in the compacted YSZ nanopowders.

Intensity ratios, I_3:I_2 , obtained from LT spectra decompositions for Zr3Y0.3Cr, Zr3Y0.7Cr and Zr3Y2.9Cr were also plotted in Fig. 4 as a function of the inverse square of mean particle size, d^{-2}. It can be seen from the Figure that these data items fall close along the straight line given by Eq. 1 Note that quotient q^2 was deduced from an independent data. In this way, a further support to the adopted interpretation of these LT components is received. Moreover, the predictive power of Eq. 1 for estimates of the mean particle sizes from LT data may be regarded to be practicable also for the ternary YSZ nanopowders. A decrease of the mean particle size with increasing chromia content is indicated by the data points of the Figure.

Contrary to the case of the binary YSZ compacted nanopowders, no Ps contribution to the LT spectra was detected [15,17] in the ternary *t*-YSZ nanopowders, even when the amount of the chromia additive was as low as 0.3 mol.%. Such a strong suppression of Ps contribution can result from a presence of the paramagnetic Cr^{5+} cations which existence has been proven, behind the Cr^{3+} main oxidation state, by X-ray photoelectron spectroscopy (XPS) [2,18]. Cr^{5+} cations act as donors which introduce quasi-free electrons into the lattice. Positrons may become chemically bound to the donors, or Ps atoms may be quickly dissociated in collisions with these electrons. One can note that a possible chemical quenching of oPs induced by Cr^{3+} electron scavengers was considered as a possible cause of Ps inhibition in Al_2O_3–Cr_2O_3 catalysts [38]. In any case, since Ps is localised only in open volumes among nanoparticles and can thus collide only with electrons or ions at the nanoparticle surface, the suppression of the Ps contribution in the LT spectra of ternary *t*-YSZ nanopowders may be regarded as strong evidence that Cr ions are segregated at the GB's.

CDB measurements. All DBP ratios mesured for the ternary *t*-YSZ compacted nanopowders, exhibit again a pronounced maximum at electron momentum $p \approx 15 \times 10^{-3}\ m_0c$, which represents positron annihilations with the oxygen electrons. However, the contribution of the electrons in the DBP ratios for the ternary YSZ nanopowders is reduced compared to that for the Zr9Y single crystal and the oxygen peak is slightly higher than that observed for the binary *t*-YSZ nanopowder (Zr3Y specimen). Unfortunately, it seems impossible to detect an effect of chromia doping on DBP ratios (if any) since the CDB response to the well-annealed pure Cr displays a peak localised at a close proximity to that of oxygen electrons.

Contrary to the situation for the Zr3Y specimen, no enhancement of DBP ratio around $p \approx 0$ was observed in the ternary *t*-YSZ nanopowders with chromia. This finding is in accordance with the LT data and results from an absence of a visible pPs contribution to the DBP ratios in the ternary *t*-YSZ nanopowders. Moreover, it practically excludes oPs spin conversion as a reason for the disappearance of oPs components in LT spectra.

Sintered YSZ ceramics. *LT measurements.* Two LT components were identified below 0.5 ns in the binary *t*-YSZ ceramics sintered at T_S = 1000 and 1200 °C, see Table 2. These two components exhibited lifetimes similar to those observed on binary YSZ compacted nanopowders. Thus it is substantiated that saturated positron trapping takes place in binary *t*-YSZ sintered ceramics and the kind of defects responsible for trapping remains the same as in binary YSZ compacted nanopowders: (i) vacancy-like misfit defects situated on grain surface and (ii) triple points. A pronounced decrease in the I_3:I_2-ratio with rising sintering temperature seen in Table 1 and Fig. 4 manifests a significant grain growth induced by sintering and accompanied by disappearance of triple points. However, at T_S = 1200 °C, a contribution originated from positron trapping at defects located in grain interiors can be expected to interfere. A decrease in defect concentration connected with grain growth is further demonstrated at T_S = 1350 °C, where even a weak short-lived component with $\tau_1 \approx 40$ ns appears, evidencing that saturated trapping does no more take place. No long-lived components with lifetimes above 1 ns could be resolved in the LT spectra of sintered materials. Hence, Ps formation is strongly suppressed compared to the compacted nanopowders. This is in accord with sintering induced particle growth which is also accompanied by disappearance of pores. An analogous muting of oPs components was seen in similar sintered YSZ ceramics by other authors [39].

In the ternary *t*-YSZ ceramics sintered at T_S = 1350 °C, saturated positron trapping is no more the case (see Table 2) because the shortest component observed ($\tau_1 \approx 0.035$ ns, $I_2 \approx 5$ %), which appeared to be of much lower lifetime than that calculated for the perfect lattice (Table 4), unambiguously originates from delocalised positrons. The dominating positron trap is the vacancy-like defect characterised with lifetime $\tau_2 \approx 0.176$ ns and intensity $I_2 \approx 90$ %. Note that τ_2-value is very close to that observed for the YSZ single crystal and slightly lower than values observed in most compacted nanopowders. The last component resolved in the ternary *t*-YSZ ceramics ($\tau_3 \approx 0.375$ ns, $I_3 \approx 5$ %) obviously represents traces of triple points that disappeared due to grain growth during sintering. Contrary to the ternary YSZ nanopowders, LT data obtained for the ternary *t*-YSZ ceramics are mutually closely similar independently of chromia content. It again testifies [15] that Cr cations are segregated predominantly at grain boundaries and, moreover, positrons in ternary *t*-YSZ ceramics sintered at 1350 °C annihilate mainly in grain interiors as trapped in vacancy-like defects similar to those which were identified [10] to be responsible for positron trapping in YSZ single crystal. These defects were moreover shown in [10] to possess size and chemical surroundings resembling V_{Zr}''''. Such a picture is further supported by a reasonable agreement of bulk lifetimes deduced from experimental data by applying simple 3-state trapping model with calculated lifetimes for the perfect zirconia lattice [15].

CDB measurements. DBP ratios measured for binary *t*-YSZ ceramics sintered at T_S = 1000 and 1200 °C approached that obtained for YSZ single crystal. This result is consistent with a grain growth picture suggested by LT data. In addition, the observation of no enhancement of the ratios in the low momentum region should be regarded as result of suppression of Ps formation in ceramics sintered at these temperatures. The amplitude of the peak originating from positron annihilation with the oxygen electrons is raised with increasing T_S . This effect may be likely attributed to an increased fraction of positron annihilations in defects inside grains.

SPIS measurements. As one can see from *S*-parameters measured recently by means of SPIS for the binary *t*-YSZ sintered ceramics vs. positron energy, plotted in Fig. 3, well pronounced variations in the measured curves could be revealed for different sintering temperatures [16]. Ps formation in the virgin (non-sintered) nanopowder is clearly visible in the Figure as well as general drop of *S*-parameters toward the single crystal values confirming a decrease in concentration of defects associated with the grain boundaries which is due to the grain growth induced by sintering at higher

temperatures. The most striking feature is, however, a clear identification of a subsurface layer of about 20 nm thickness which contains a relatively high concentration of defects and was tentatively attributed [16] to defect diffusion from the sample interior toward its surface. Sintering-induced sample surface modifications may also be in effect, however, as suggested by a remarkable T_S-dependent increase of S-parameters taken for lowest positron energies.

Summary and concluding remarks

The present status of systematic PAS investigations on a variety of binary and ternary (with chromia additive) YSZ nanomaterials, being performed in the frame of the Prague – Rossendorf – Donetsk collaboration, have been reviewed. These investigations have allowed drawing of the following main conclusions:

- Among various vacancy-like defect configurations which can be expected in the YSZ lattice, only V_{Zr}'''' were suggested by the state-of-art theoretical analysis to be capable of positron trapping, even in case that a hydrogen atom is attached to the zirconium vacancy.
- Strong evidence is provided by the LT, CDB and SPIS measurements combined with theoretical calculations of positron parameters that positrons in the *c*-YSZ single crystal are trapped in vacancy-like defects which size and chemical surroundings resemble that of V_{Zr}''''.
- Positrons in the YSZ compacted nanopowders were shown by the LT data to annihilate as trapped in two kinds of open-volume defects: (i) in vacancy-like misfit defects similar to V_{Zr}'''', which are situated along GB's, and (ii) in triple points – the intersections of three or more GB's which exhibit an open volume equivalent to a cluster of a few vacancies. Moreover, ≈ 10 % of positrons was found to form Ps in the compacted binary YSZ nanopowders in pores of ≈ 3 nm size occurring between the primary particles.
- The intensity ratio of LT components corresponding to the triple points and vacancy-like defects was proven to be linearly correlated with the inverse square of the mean particle size derived from XRD shape analysis. This finding is consistent with the adopted interpretation of these components and can serve for an estimate of the mean grain size or its relative change using the LT data only.
- In the ternary *t*-YSZ compacted nanopowders, the mean grain size was shown to slightly decrease with increasing chromia content.
- In the binary YSZ sintered ceramics, a substantial grain growth was detected by LT data not only as a disappearance of the Ps components, but also as a sharp drop of the intensity of the triple point component.
- Cr cations cause a substantial inhibition of Ps formation which was clearly proven by the LT measurements in all the ternary *t*-YSZ compacted nanopowders doped with chromia. The presence of a fraction of Cr^{5+} cations observed in XPS measurements was suggested as a cause of this phenomenon. Ps inhibition simultaneously brings a strong evidence of Cr segregation along GB's. Such segregation is also supported by present CDB results.

The SPIS technique was applied to binary YSZ sintered ceramics. It displayed some well-pronounced trends in microstructure evolution which obviously take place during sintering. To authors' knowledge, this technique has yet been only scarcely utilised in nanomaterials studies and, undoubtedly, it is worthy of greater effort in future studies.

The present experiments illustrate that conventional PAS may become an important complementary technique to SPIS in surface studies on nanomaterials. This is because the power of the conventional PAS to gain information on internal surfaces is strongly enhanced due a significantly enlarged volume fraction of GB's in nanomaterials.

Acknowledgements

This review was made under financial support granted by The Czech Scientific Foundation within contract GA P108/11/1396 and by The Czech Academy of Sciences within project KAN 300100801. Partial financial support from The Ministry of Education, Youths and Sports of the Czech Republic (project "Mobility" MEB 101102) and German Academic Exchange Service (project 71 31 308 022) is also acknowledged. Further financial support of this work was obtained from The National Academy of Sciences of Ukraine within the Complex programme of fundamental research of NAS Ukraine "Fundamental problems of nanostructured systems, nanomaterials and nanotechnologies" (project 89/12-H).

References

[1] S.P. Badwal, M.J. Bannister, R.H.J. Hannink (Eds.), Science and Technology of Zirconia V, Technomic Pub. Co., Lancaster, Pennsylvania, 1993.

[2] I.A.Yashchishyn, A.M. Korduban, V.V. Trachevskiy, T.E. Konstantinova, I.A. Danilenko, G.K. Volkova, I.K. Nosolev, XPS and ESR spectroscopy of ZrO_2-Y_2O_3-Cr_2O_3 nanopowders, Functional Materials **17** (2010) 306-310.

[3] P. Hautojärvi, C. Corbel, Positron spectroscopy of defects in metals and semiconductors, in: A.P. Mills, Jr., and A. Dupasquier (Eds.), Positron spectroscopy of solids, Proc. Internat. School of Physics «Enrico Fermi», Course CXXV, IOS Press, Amsterdam, 1995, pp. 491-532.

[4] R. Krause-Rehberg, H.S. Leipner, Positron Annihilation in Semiconductors: Defect Studies, Springer Series in Solid State Science 127, Springer Verlag, Berlin, Heidelberg, New Jersey, 1999, pp. 5-48.

[5] A. Van Veen, H. Schut, E.P. Mijnarends, Depth profiling of subsurface regions, interfaces and thin films, in: P. Coleman (editor), Positron beams and their applications, World Scientific, Singapore, 2000, pp. 191-226.

[6] J. Cizek, O. Melikhova, J. Kuriplach, I. Prochazka, T.E. Konstantinova, I.A. Danilenko, Defects in yttria-stabilized zirconia: a positron annihilation study, phys. stat. sol (c) **4** (2007) 3847-3850.

[7] O. Melikhova, J. Kuriplach, J. Cizek, I. Prochazka, G. Brauer, W. Anwand, T.E. Konstantinova, I.A. Danilenko, Positron annihilation in three zirconia polymorphs, phys. stat. sol. (c) **4** (2007) 3831-3834.

[8] I. Prochazka, J. Cizek, J. Kuriplach, O. Melikhova, T.E. Konstantinova, I.A. Danilenko, Positron Lifetimes in Zirconia-Based Nanomaterials, Acta Phys. Polonica A **113** (2008) 1495-1499.

[9] J. Cizek, O. Melikhova, J. Kuriplach, I. Prochazka, T.E. Konstantinova, I.A. Danilenko, Sintering of yttria-stabilized zirconia nanopowders studied by positron annihilation spectroscopy, Phys. Status Solidi C **6** (2009) 2582-2584.

[10] J. Cizek, O. Melikhova, I. Prochazka, J. Kuriplach, R. Kuzel, G. Brauer, W. Anwand, T.E. Konstantinova, I.A. Danilenko, Defect studies of nanocrystalline zirconia powders and sintered ceramics, Phys. Rev. B **81** (2010) art. 024116.

[11] O. Melikhova, J. Kuriplach, J. Cizek, I. Prochazka, G. Brauer, W. Anwand, Investigation of hydrogen interaction with defects in zirconia, Journ. of Phys.: Conf. Ser. **225** (2010) art. 012035.

[12] O. Melikhova, J. Kuriplach, J. Cizek, I. Prochazka, G. Brauer, W. Anwand, Investigation of hydrogen interaction with defects in zirconia, Mater. Res. Soc. Symp. Proc. Vol. **1216** (2010) 1216-W07-10.

[13] I. Prochazka, J. Cizek, O. Melikhova, J. Kuriplach, T.E. Konstantinova, I.A. Danilenko, Positron annihilation study of yttria-stabilized zirconia nanopowders containing Cr_2O_3 additive, Journ. of Phys.: Conf. Ser. **265** (2011) art. 012020.

[14] O. Melikhova, J. Cizek, J. Kuriplach, I. Prochazka, W. Anwand, G. Brauer, D. Grambole, Characterization of point defects in yttria stabilized zirconia single crystals, Journ. of Phys.: Conf. Ser. **262** (2011) art. 012038.

[15] O. Melikhova, J. Cizek, I. Prochazka, T.E. Konstantinova, I.A. Danilenko, Defect studies of yttria stabilized zirconia with chromia additive, Phys. Procedia (2011) accepted for publication.

[16] I. Prochazka, J. Cizek, O. Melikhova, W. Anwand, G. Brauer, T.E. Konstantinova, I.A. Danilenko, Effect of Sintering on Defects in Yttria Stabilised Zirconia, Mater. Sci. Forum (2012) accepted for publication.

[17] O. Melikhova, J. Cizek, I. Prochazka, J. Kuriplach, T.E. Konstantinova, I.A. Danilenko, Quenching of positronium formation in yttria stabilized zirconia nanopowders modified by addition of chromia, Mater. Sci. Forum (2012) accepted for publication.

[18] I.A.Yashchishyn, A.M. Korduban, T.E. Konstantinova, I.A. Danilenko, G.K. Volkova, V.A. Glazunova, V.O. Kandyba, Structure and surface characterization of ZrO_2-Y_2O_3-Cr_2O_3 system, Appl. Surf. Sci. **256** (2010) 7174-7177.

[19] T. Konstantinova, I. Danilenko, V. Glazunova, G. Volkova, O. Gorban, Mesoscopic phenomena in oxide nanoparticle systems: processes of growth, Journ. Nanopart. Res. **13** (2011) 4015-4023.

[20] F. Becvar, J. Cizek, L. Lestak, I. Novotny, I. Prochazka, F. Sebesta, A high-resolution BaF_2 positron-lifetime spectrometer and experience with its long-term exploitation, Nucl. Instr. Meth. in Phys. Research A **443** (2000) 557-577.

[21] F. Becvar, J. Cizek, I. Prochazka, J. Janotova, The asset of ultra-fast digitizers for positron-lifetime spectroscopy, Nucl. Instr. Meth. in Phys. Research A **539** (2005) 372-385.

[22] I. Prochazka, I. Novotny, F. Becvar, Application of Maximum-Likelihood Method to Decomposition of Positron-Lifetime Spectra to Finite Number of Components, Mater. Sci. Forum **255-257** (1997) 772-774.

[23] J. Cizek, M.Vlcek, I. Prochazka, Digital spectrometer for coincidence measurements of of Doppler broadening of positron annihilation radiation, Nucl. Instr. Meth. in Phys. Research A **623** (2010) 982-994.

[24] W. Anwand, H.-R. Kissener, G. Brauer, A magnetically guided slow positron beam for defect studies, Acta Phys. Polonica A **88** (1995) 7-11.

[25] A. Van Veen, H. Schut, J. de Vries, R.A. Hakwoort, M.R. Ijpma, Analysis of positron profiling data by means of "VEPFIT", in: P.J. Schultz, G.R. Massoumi, P.J. Simpson (Eds.), Positron Beams for Solids and Surfaces, AIP Conf. Proc., Vol. **218**, American Institute of Physics, New York, 1990, pp. 171-198.

[26] F.A. Kröger, Chemistry of Imperfect Crystals, Vol. 2, first ed., North-Holland, Amsterdam, 1974.

[27] M.J. Puska, R.M. Nieminen, Defect spectroscopy with positrons: a general calculational method, J. Phys. F: Metal Phys. **13** (1983) 333-346.

[28] A.P. Seitsonen, M.J. Puska, R.M. Nieminen, Real-space electronic structure calculations: Combination of the finite difference and conjugate gradient methods, Phys. B **51** (1995) 14057-14061.

[29] E. Boroński, R.M. Nieminen, Electron-positron density-functional theory, Phys. Rev. B **34** (1986) 3820-3831.

[30] B. Barbiellini, M.J. Puska, T. Torsti, R.M. Nieminen, Gradient correction for positron states in solids, Phys. Rev. B **51** (1995) 7341-7344.

[31] G. Kresse, J. Furthmüller, Efficiency of ab-initio total energy calculations for metals and semiconductors using a plane-wave basis set, Comput. Mater. Sci. **6** (1996) 15-50.

[32] G. Kresse, J. Hafner, Ab-initio molecular-dynamics for liquid crystals, Phys. Rev. B **47** (1993) 558-561.

[33] M. Alatalo, B. Barbielini, M. Hakala, H. Kauppinen, T. Korhonen, M.J. Puska, K. Saarinen, P. Hautojärvi, R.M. Nieminen, Theoretical and experimental study of positron annihilation with core electrons in solids, Phys. Rev. B **54** (1996) 2397-2409.

[34] J. Kuriplach, A.L. Morales, C. Dauwe, D. Seghers, M. Sob, Vacancies and vacancy-oxygen complexes in silicon: Positron annihilation with core electrons, Phys. Rev. B **58** (1998) 10475-10483.

[35] R.I. Grynszpan, S. Saude, L. Mazerolles, B. Brauer, W. Anwand, Positron depth profiling in ion implanted zirconia stabilized with trivalent cations, Radiat. Phys. Chem. 76 (2007) 333-336.

[36] K. Ito, Y. Yagi, S. Hirano, M. Miyayama, T. Kudo, A. Kishimoto, Y. Ujihira, Estimation of Pore Size of Porous Materials by Positron Annihilation Lifetime Measurement, J. Ceram. Soc. Japan **107** (1999) 123-127.

[37] K. Ito, H. Nakanishi, Y. Ujihira, Extension of the Equation for the Annihilation Lifetime of *ortho*-Positronium at a Cavity larger than 1 nm in Radius, J. Chem. Phys. B **103** (1999) 4555-4558.

[38] Sh. Huang, Y. Dai, H. Zhang, Z. Chen, Chemical Quenching and Inhibition of Positronium in Cr_2O_3/Al_2O_3 Catalysts, Wuhan Univ. Journ. Nat. Sci. **16** (2011) 308-312.

[39] Y. Yagi, S. Hirano, Y. Ujihira, M. Miyayama, Analysis of the sintering process of 2 mol% yttria-doped zirconia by positron annihilation lifetime measurements, J. Mater. Sci. Letts. **18** (1999) 205-207.

Near-Surface Depth Profiling of Solids by Mono-Energetic Positrons
10.4028/www.scientific.net/DDF.331

Defect Behaviour in Yttria-Stabilised Zirconia Nanomaterials Studied by Positron Annihilation Techniques
10.4028/www.scientific.net/DDF.331.181